# Design and optimization of dispersion-flattened microarray-core fiber with ultralow loss for terahertz transmission

**Lei Zhang** [a,b], **Wanli Luo** [a,b], **Jing Bai** [c,d], **Haiping Bai** [e], **Peng Jiang** [a,b], **Qiang Xu** [a,b,f,*], **Kang Li** [f], **Nigel Copner** [f], **Yongkang Gong** [g]

[a] *College of Physics and Optoelectronic Technology, Baoji University of Arts and Sciences, Baoji 721016, China*
[b] *Engineering Technology Research Center for Ultrafast Optics and Advanced Material of Baoji, Baoji 721016, China*
[c] *College of Mechanical Engineering, Baoji University of Arts and Sciences, Baoji 721016, China*
[d] *Baoji Engineering Research Center of Robot Testing and Measurement, Baoji,721016, China*
[e] *College of Science, Inner Mongolia Agricultural University, Hohhot 010018, China*
[f] *Wireless and Optoelectronics Research and Innovation Centre, Faculty of Computing, Engineering and Science, University of South Wales, CF37 1DL, United Kingdom*
[g] *School of Physics and Astronomy, Cardiff University, CF24 3AA, United Kingdom*

**Abstract** The paper establishes a late-model of microarray-core based polymer optical fiber with flattened dispersion and ultra-low losses. Its transmission properties are calculated by virtue of the beam propagation approach. From the simulation results, it finds that the modelled fiber has a near-zero dispersion property of $0.29 \pm 0.16$ ps/THz/cm in a frequency area of 1.05 THz to 1.78 THz, a high birefringence of $1.6 \times 10^{-3}$, an ultra-low confinement loss of $3.78 \times 10^{-10}$ dB/m, an effective mode field zone of $4.6 \times 10^5$ $\mu m^2$, and a nonlinear coefficient of 1.2 $km^{-1} \cdot W^{-1}$. With these good properties, the modelled fiber could be applied for ethanol detection and polarization maintaining THz applications.

## 1. Introduction

While the computational performance of mobile devices improves, the applicability of smart IoT applications, such as

smart homes and smart factories has become the trend [1]. The related terahertz (THz) radiation spectroscopy has also become a research hotspot. Terahertz (THz) radiation spectrum (0.1–10 THz) is an electromagnetic wave that exists between microwave and infrared radiation. The special spectral position of the THz wave has advantages different from other electromagnetic radiation, such as perspectivity, signal-to-noise ratio, spectral resolution and security and so on [2].

Based on the main characteristics of THz wave, THz has very significant applications in THz tomography [3], biomedical sensing [3,4], radar detection [5], wireless communication [6,7], nondestructive testing [8], Travelling Sales Problem (TSP) [63], and other fields.

The waveguide-structured THz functional device is very fundamental device to generate other application functions. Therefore, it is of great importance to develop an all-fiber THz system with strong power and adaptability. Meanwhile, THz technology has seen great achievements in optical fiber technology with low-loss. For instance, it is used to generate a large variety of functional devices, such as polarization controller [9,10], filter [11,12], optical switch [13], THz wave directional coupler [14,15], beam splitter [16,17] and etc. One of these devices is a porous core fiber-based THz fiber device, which, as a vital element in the application research of THz technology, has a very wide application prospect in THz communication and sensing system [10,18-21]. Li et al. (2019) proposed a decentralized on-demand energy supply approach based on micro-grids to provide decentralized on-demand energy for mining in IoT devices [64]. THz wave can be easily taken in by dielectric objects, so for THz wave transmission research, it usually selects such similar materials with less losses. To decrease a particular material's loss of absorption, good background materials and photonic crystal fiber (PCF) like the porous or hollow photonic crystal fiber [22,23] are used.

Since Knight et al introduced the photonic crystal fiber (PCF) [24,25], its distinctive characteristics, like the high birefringence [26-28], dispersion management [29], high nonlinear coefficient [30], endlessly single mode [31], flexibility of design and so on, have aroused the great interest of the scientist. High birefringence is achieved by enlarging the disparity between the effective refractive index of x-polarization mode and y-polarization of PCF, while high birefringence could prevent any change to the subsisting linear polarization state in the fiber [26-28,32]. As a rule of law, high birefringence could be obtained by bringing into use the asymmetric defect structure of cladding and fiber core. Ferrando et al found that rectangular lattice PCF has a stronger geometric anisotropy than honeycomb and triangular PCF [32]. Dispersion characterizes the operational capability of optical fiber in multi-channel communication applications [33]. 5G provides high coverage and very high frequency by deploying dense base station (BS) with enhanced quality, extremely low latency and increased capacity [63]. In the optical fiber communication system, the transmission information is mainly transmitted through the encoded optical pulse train on the optical fiber. Dispersion-flattened Fibers are advantageous to broadband flat supercontinuum generation and optical frequency conversion. However, high dispersion at a specific wavelength will lead to strong instability of the soliton system, which will eventually destroy the transmission characteristics of the soliton pulse [29,30]. Hence, Dispersion, nonlinearity and birefringence play a momentous role in transmission of optical pulse in optical fiber.

At present, beam propagation method (BPM) [34-38], multi-pole method [39-41], full vector finite element method (FV-FEM) [42-44], effective index method [45,46], plane wave method [47,48], and finite difference time domain method [49,50] will be adopted to study the transmission characteristics of THz-PCFs. BPM is the most widely used one to simulate electromagnetic wave propagation in integrated and optical devices. Main reasons for the popularity of BPM [34-38]: (1) the physical concept of BPM is simple and allows for the rapid implementation of basic technologies. (2) BPM is a very efficient approach, and in most cases, computational complexity is optimal. (3) BPM can be easily applied to complex geometries without the need to develop a specialized version of the approach. (4) BPM can also automatically consider the effects of both coupling and conversion mode as well as radiating and guided fields. (5) BPM technologies are very flexible and extensible, allowing the basic approach to be extended within the same overall framework.

PCFs provides a high-quality microfluidic channel for excellent optical performance by filling the microarray-core with different functional materials. Ethanol is a kind of very crucial raw material of the industry that is widely used in the fields of food, chemistry, medicine, military application and etc. [51,52]. How to fast and accurately identify the components of ethanol is of great significance. The design of an ethanol-based microarray core PCF will provide the basis for further terahertz fiber sensing.

Therefore, based on the aforementioned analysis, the motivation of this study is to design a dispersion-flattened microarray-core PCF with ultralow loss for THz transmission. In this paper, a numerical simulation of a TOPAS®-based rectangular PCF is presented using BPM [53-55]. The novelty of design is introduced by applying elliptical hole microarray core based on alcohol filling inside a rectangular lattice. The designed PCF shows a near-zero dispersion of $0.29 \pm 0.16$ p s/THz/cm, a high birefringence of $1.6 \times 10^{-3}$, an ultra-low confinement loss of $3.78 \times 10^{-10}$ dB/m. In addition, the effective mode field zone and nonlinear coefficient are $4.6 \times 10^5$ $\mu m^2$ and $1.2$ km-1·W$^{-1}$ respectively. It is predicted that this late-model THz PCF will have a vital application prospect in THz transmission and sensing fields such as dispersion management and polarization maintaining.

## 2. Principles and methods

Fig. 1 is the cross section of the designed THz PCF with an ethanol filled elliptical microarray-core. The polymer structure consists of a rectangular array of air holes cladding and an elliptical microarray-core. The elliptical microarray-core is brought into to induce high birefringence by virtue of changing the geometrical symmetry of the fiber. It is worth noting that the periodicity in the hole array is not wholly needed due to the fact that the light transmitted herein is total internal reflection rather than the photonic bandgap guidance. The substrate material is the polymer TOPAS with a refractive index of 1.53 [53-55]. The refractive index of the air holes of proposed porous THz PCF is 1.00. The elliptical microarray-core was filled with an alcohol solution with a refractive index of 1.354. The cladding of proposed THz PCF is composed of circular air holes with a diameter of d, that are surrounded by 5 rectangular lattice rings. Period $\Lambda$ denotes the distance between any two adjacent air holes. The air-filling ratio of the cladding is d/$\Lambda$. The elliptical microarray-core is composed of a center ellipse and eight ellipses which are symmetrically distributed on either side. Minor and major axes of the ellipse are fixed and denoted respectively by w and Li (i = 1, 2, 3, 4, 5).
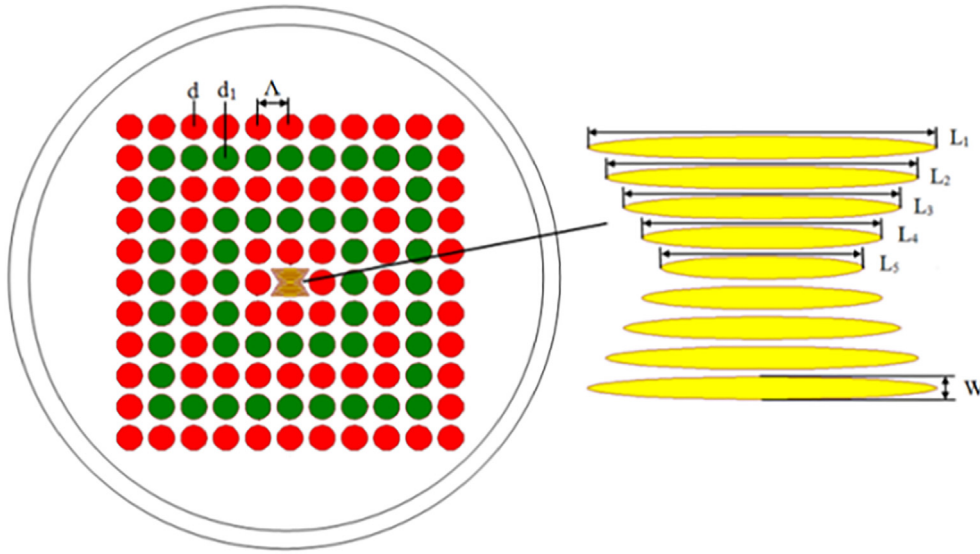
**Fig. 1** Cross section with enlarged core of the designed THz PCF.

The BMP [34-38] is the most popular tool to be used to study the light propagation in longitudinally varying waveguides. According to Maxwell's equations, the vector wave equation for the time-harmonic electric field in a time-invariant, isotropic, dielectric, non-homogeneous, and linear medium is derived as

$$\nabla \times \overrightarrow{E} = -i\omega\mu \overrightarrow{H} \tag{1}$$

$$\nabla \times \overrightarrow{H} = i\omega\varepsilon \overrightarrow{E} \tag{2}$$

$$\nabla \cdot \overrightarrow{D} = 0 \tag{3}$$

$$\nabla \cdot \overrightarrow{B} = 0 \tag{4}$$

where $\overrightarrow{E}$ and $\overrightarrow{H}$ denote the effective refractive index of x-polarization and y-polarization, respectively.

$\overrightarrow{D} = \varepsilon \overrightarrow{E}$ and $\overrightarrow{B} = \mu \overrightarrow{H}$ represent the electric displacement vector and magnetic induction, respectively. $\omega$ is angular frequency, $\varepsilon$ and $\mu$ represent the permittivity and permeability, respectively.

The general solutions to Eqs. (1) and (2) can be expressed as

$$\nabla \times \nabla \times \overrightarrow{E} = \nabla(\nabla \cdot \overrightarrow{E}) - \nabla^2 \overrightarrow{E} = n^2 k_0^2 \overrightarrow{E} \tag{5}$$

The Eq. (5) is Helmholtz equation, where $n = (\mu\varepsilon/\mu_0\varepsilon_0)^{1/2}$ represents the refractive index of the isotropic medium, $k_0 = 2\pi/\lambda_0$ is the wave number in vacuum, $\lambda_0$ is free space wavelength, $\varepsilon_0$ and $\mu_0$ represent the permittivity and permeability in vacuum, respectively.

The $z$ is the propagation direction, and $x$- and $y$- are the transverse dimensions, $x$- and $y$- components of Eq. (5) can be expressed as

$$\nabla^2 E_x + n^2 k^2 E_x = \nabla_x \left( \nabla_x \cdot E_x + \frac{\partial E_z}{\partial z} \right) \tag{6a}$$

$$\nabla^2 E_y + n^2 k^2 E_y = \nabla_y \left( \nabla_y \cdot E_y + \frac{\partial E_z}{\partial z} \right) \tag{6b}$$

Eq. (3) can be transformed into Eq. (7a), and (7b)

$$\nabla_x \cdot \left( n^2 E_x \right) + \frac{\partial n^2}{\partial z} E_z + n^2 \frac{\partial E_z}{\partial z} = 0 \tag{7a}$$

$$\nabla_y \cdot \left( n^2 E_y \right) + \frac{\partial n^2}{\partial z} E_z + n^2 \frac{\partial E_z}{\partial z} = 0 \tag{7b}$$

When the refractive index changes very slowly along the direction of light wave transmission, the $\frac{\partial n^2}{\partial z} E_z$ can be ignored. Based on the above considerations, Eqs. (7a) and (7b) are substituted into Eqs. (6a) and (6b) respectively

$$\nabla^2 E_x + n^2 k^2 E_x = -\frac{\partial}{\partial x} \left( \frac{\partial \ln n^2}{\partial x} E_x + \frac{\partial \ln n^2}{\partial y} E_y \right) \tag{8a}$$

$$\nabla^2 E_y + n^2 k^2 E_y = -\frac{\partial}{\partial y} \left( \frac{\partial \ln n^2}{\partial x} E_x + \frac{\partial \ln n^2}{\partial y} E_y \right) \tag{8b}$$

Assumption

$$E_j = A_j \exp(-iskn_0 z) \tag{9}$$

where $n_0$ is a reference refractive index. Based on the Slowly Varying Envelope Approximation (SVEA),

$$\left| \frac{\partial^2 A_j}{\partial z^2} \right| << 2n_0 k_0 \left| \frac{\partial A_j}{\partial z} \right| \tag{10}$$

substituting Eq. (9) into Eq. (8a) and (8b), we obtained the paraxial vector wave equations for BPM:

$$is\frac{\partial A_x}{\partial z} = \frac{1}{2k_0 n_0} \left[ \frac{\partial^2 A_x}{\partial x^2} + \frac{\partial^2 A_x}{\partial y^2} + k_0(n^2 - n_0^2)A_x + \frac{\partial}{\partial x}\left( A_x \frac{\partial \ln n^2}{\partial x} + A_y \frac{\partial \ln n^2}{\partial y} \right) \right] \tag{11a}$$

$$is\frac{\partial A_y}{\partial z} = \frac{1}{2k_0 n_0} \left[ \frac{\partial^2 A_y}{\partial x^2} + \frac{\partial^2 A_y}{\partial y^2} + k_0(n^2 - n_0^2)A_y + \frac{\partial}{\partial y}\left( A_x \frac{\partial \ln n^2}{\partial x} + A_y \frac{\partial \ln n^2}{\partial y} \right) \right] \tag{11b}$$

Considering a planar structure, invariant in the $x$- or $y$- direction, so that $\partial/\partial x = 0$ or $\partial/\partial y = 0$, the equations decouple and solutions have $TE$ and $TM$ polarizations. The Eqs. (11a) and (11b) can be reduced to

$$is\frac{\partial A_x}{\partial z} = \frac{1}{2k_0n_0}\left[\frac{\partial^2 A_x}{\partial x^2} + \frac{\partial^2 A_x}{\partial y^2} + k_0(n^2 - n_0^2)A_x\right] \tag{12a}$$

$$is\frac{\partial A_y}{\partial z} = \frac{1}{2k_0n_0}\left[\frac{\partial^2 A_y}{\partial x^2} + \frac{\partial^2 A_y}{\partial y^2} + k_0(n^2 - n_0^2)A_y\right] \tag{12b}$$

If we propagate along the imaginary axis $iz$, the paraxial wave equation becomes

$$\frac{\partial A_j}{\partial z} = \hat{N}A_j \tag{13}$$

where $j = x, y$ and

$$\hat{N} = \frac{1}{2sk_0n_0}\left[\frac{\partial^2 A_y}{\partial x^2} + \frac{\partial^2 A_y}{\partial y^2} + k_0(n^2 - n_0^2)\right] \tag{14}$$

where the propagation direction parameter $s$ is defined as

$$s = \begin{cases} +1 & \text{for} \quad +z \quad \text{direction} \\ -1 & \text{for} \quad +z \quad \text{direction} \end{cases} \tag{15}$$

Similarly, equations for magnetic fields can be derived in the same way. The vector waves may be decomposed into the $TE$ and $TM$ polarizations which can be treated by solving (13). Further solutions are given by using the so-called perfectly matched layers (PMLs) boundary conditions [37,38]. They are based on the transformation of a factor $(1 - j\sigma_e/(\omega\varepsilon_0 n^2)$ or $1 - j\sigma_m/(\omega\mu_0)$ , $\sigma_e$ and $\sigma_m$ are the electric and magnetic conductivities of PML, respectively) of each transversal coordinate in Maxwell's equations in a region external to the useful computational window. In this domain, the transmission of the field will attenuate.

The characterization of dispersion properties will be conducive to testing the capability of optical fiber multichannel communication applications. The dispersion $D(\lambda)$ of TOPAS-based THz PCF has been gotten from the $n_{eff}$ values vs. the wavelength using [29]:

$$D(\lambda) = -\frac{\lambda}{c}\frac{\partial^2\left|Re\left(n_{eff}\right)\right|}{\partial\lambda^2} \tag{16}$$

The introduction of rectangular array cladding and elliptical microarray-core in the design will cause geometrical anisotropy and asymmetrical stress, thus giving rise to different phase velocities for the two fundamental orthogonal modes. The THz fiber with high birefringence can maintain the polarization state of the transmitted light. The modal birefringence is thus denoted as [26-28]

$$B = \left|n_{eff}^x - n_{eff}^y\right| \tag{17}$$

where $n_{eff}^x$ and $n_{eff}^y$ represent the effective refractive index of $x$-polarization and $y$-polarization, respectively.

Confinement loss determines the degree of light is in the core region. Usually, confinement loss is reduced by increasing the number of rings in the cladding layer. The confinement loss of TOPAS-based THz PCF is derived from the imaginary component of the effective refractive index with the following equation [26],

Where f is the frequency, c is the light velocity, and $Im(n_{eff})$ is the imaginary component of the effective refractive index.,

$$Confinement \quad loss = \left(\frac{4\pi f}{c}\right)Im(n_{eff}) \qquad [cm^{-1}] \tag{18}$$

where $f$ is the frequency, $c$ is the light velocity, and $Im(n_{eff})$ is the imaginary part of the effective refractive index.

A low effective mode area is suitable for optical nonlinear effects, while a high effective mode area is suitable for laser communication and optoelectronic devices. Effective mode area $A_{eff}$ is calculated using [29].

$$A_{eff} = \frac{\left(\iint |E|^2 dA\right)^2}{\iint |E|^4 dA} \tag{19}$$

So, corresponding to the nonlinear coefficient $\gamma(\lambda)$ of TOPAS®-based THz PCF can be calculated by [29].

$$\gamma(\lambda) = \frac{2\pi n_2}{\lambda A_{eff}} \tag{20}$$

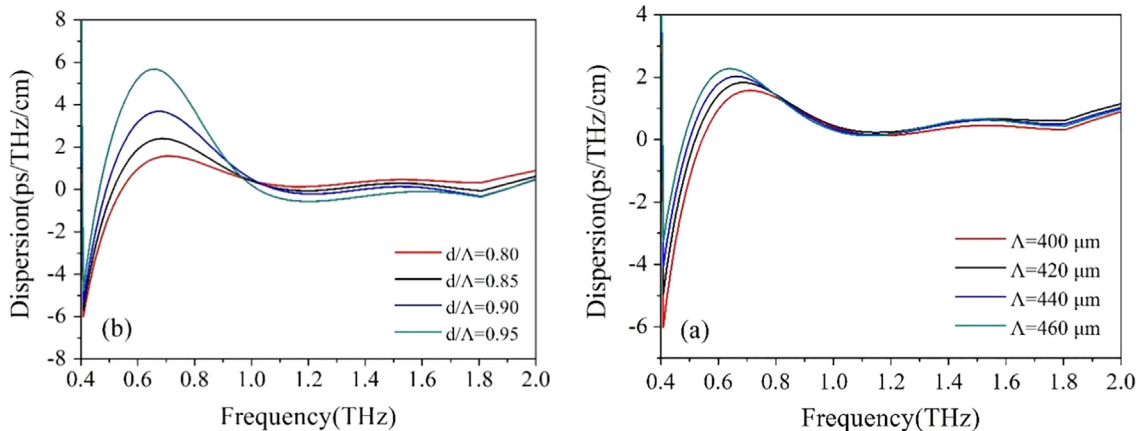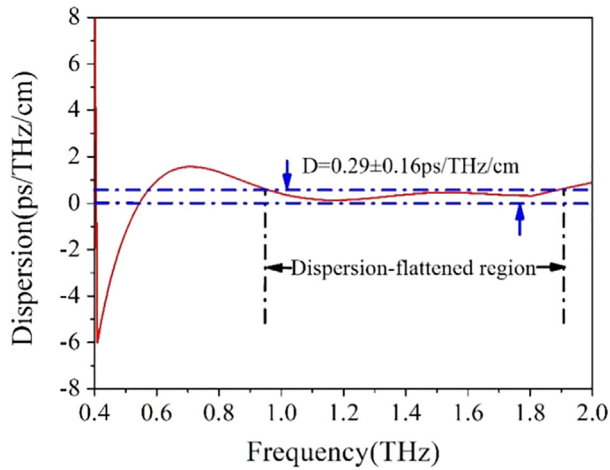where $n_2$ is nonlinear refractive index of materials. $\lambda$ is wavelength of light.



**Fig. 2**   Dispersion as a function of frequency for different (a) period $\Lambda$ and (b) air-filling ratio d/$\Lambda$.

## 3. Simulation results and analyses
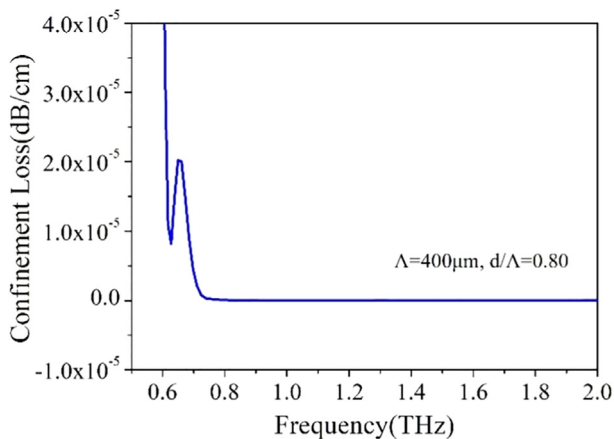
First, Fig. 2(a) shows the dispersion curves of the said PCF, a function of frequency with different period Λ, with a fixed air-filling ratio d/Λ, and when altering the value of period Λ from 400 μm to 460 μm by adding a small variable of 20 μm. Fig. 2 (a) shows that there is a nearly constant maximum dispersion for different period Λ for frequency f ≥ 0.8 THz. However, the dispersion increases gradually with period Λ. Meanwhile, it shows that all the dispersion curves adjoining each other are becoming closer, and the slope is becoming more and more similar. In order to obtain ultra-flattened dispersion, period Λ = 400 μm is selected. Next, fix Λ = 400 μm while adjusting air-filling fraction d/Λ, further analyze the slopes. Fig. 2(b) shows that dispersion increases with increasing air-filling fraction d/Λ for frequency f 1.0 THz. However, the results are opposite to the above for frequency f ≥ 1.0 THz. With the purpose of achieving an ultra-flattened dispersion, we fixed air-filling fraction d/Λ = 0.8. As per above-mentioned simulation results, it finds the most optimum design parameters of Λ =



**Fig. 3** Dispersion with respect to frequency at Λ = 400 μm, d/Λ = 0.80.
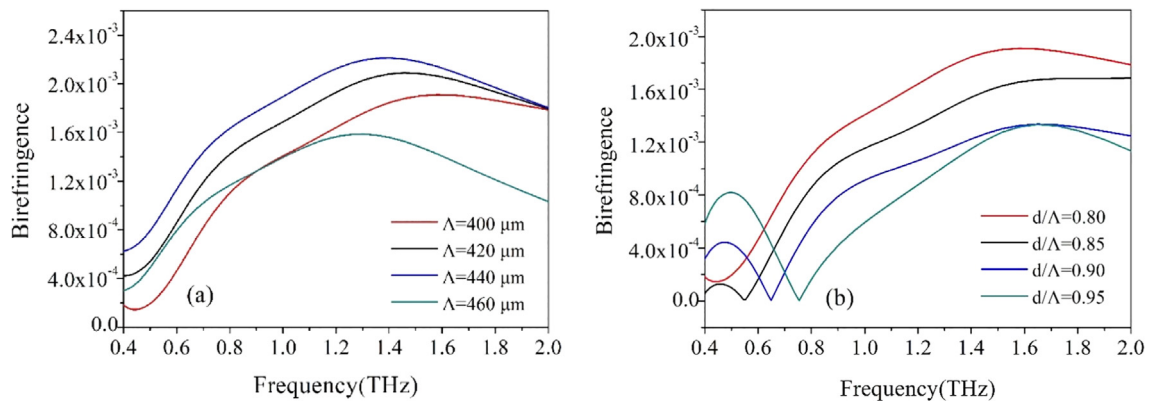


**Fig. 4** Birefringence as a function of frequency for different (a) period Λ and (b) air-filling ratio d/Λ.



**Fig. 5** Confinement loss with respect to frequency at Λ = 400 μm, d/Λ = 0.80.
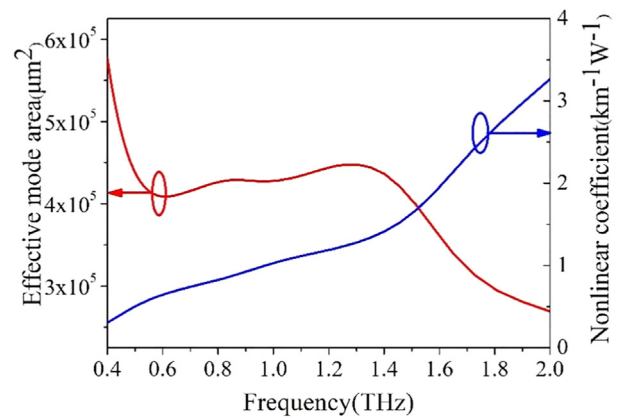


**Fig. 6** Effective mode area (a) and nonlinear coefficient (b) as a function of frequency at Λ = 400 μm, d/Λ = 0.80.

400 μm and d/Λ = 0.8. As shown in Fig. 3, the dispersion variation is within 0.29 ± 0.16 ps/THz/cm at a bandwidth of 730 GHz, which is better than previously references [6,17,30,56]. The most important property in this design is that there is an almost ultra-flattened dispersion over a wide frequency range, which is of great importance for the THz multi-channel communication.

First, we analyze the birefringence characteristics of the said PCF (a function of frequency with different Λ). From Fig. 4(a), it shows that the slope rises and falls according to the alteration of the frequency. Moreover, we can find that the value of birefringence would increases in tandem with the increasement of period Λ when Λ ≤ 440 μm. However, when Λ ≥ 440 μm, the results are opposite to the above. The reason for the above phenomenon is that at the lower period Λ, the mode field constraint is good, while at the higher period, the mode field tends to disengage from the core and to penetrate the cladding. Then Fig. 4(b) shows the frequency of birefringence. It is found that the bandwidth of birefringence decreases with increasing air-filling ratio d/Λ. The highest birefringence of $1.6 \times 10^{-3}$ is obtained for Λ = 400 μm, d/Λ = 0.80, which is better than previously reference [57]. This is because at higher frequencies, the scattering property of the fiber tends to be manifested, while the incremental rate of effective refractive index difference of the orthogonal polarization modes begins to decrease. The high birefringence of the designed fiber is extremely vital for polarization-dependent THz applications.

Fig. 5 shows the characteristics of confinement loss to frequency at a fixed Λ. It shows that confinement loss is inversely proportional to frequency. The reasons for this can be explained as that the mode field tends to be more and more restricted in the microarray-core area when the frequency increases. At optimal design conditions, the obtained confinement loss is $3.7 \times 10^{-10}$ dB/m that is higher lower compared to [56,58-61] optical waveguides.

The effective mode area refers to the area that light intensity and materials have good interaction. Be it in laser, or communication devices, it has wide application and has good optical nonlinear effects. Fig. 6 represent relationship between nonlinear coefficient and effective mode area with frequency for optimal design parameters of the proposed PCF. Fig. 6 shows that, nonlinear coefficient increases when increasing the operating frequency. Meanwhile, effective mode area decreases when increasing the operating frequency. It can be found from formula (19) that the nonlinear coefficient is correlated with the effective mode area. The larger the effective mode area is, the smaller the obtained nonlinear coefficient will be. The effective mode field area and nonlinear coefficient are $4.6 \times 10^5$ μm2 and 1.2 km-1·W-1, respectively. But, unfortunately, the effective mode area [6,57-62] and nonlinear coefficient [6,17,56-62] were often omitted in the past PCFs designs.
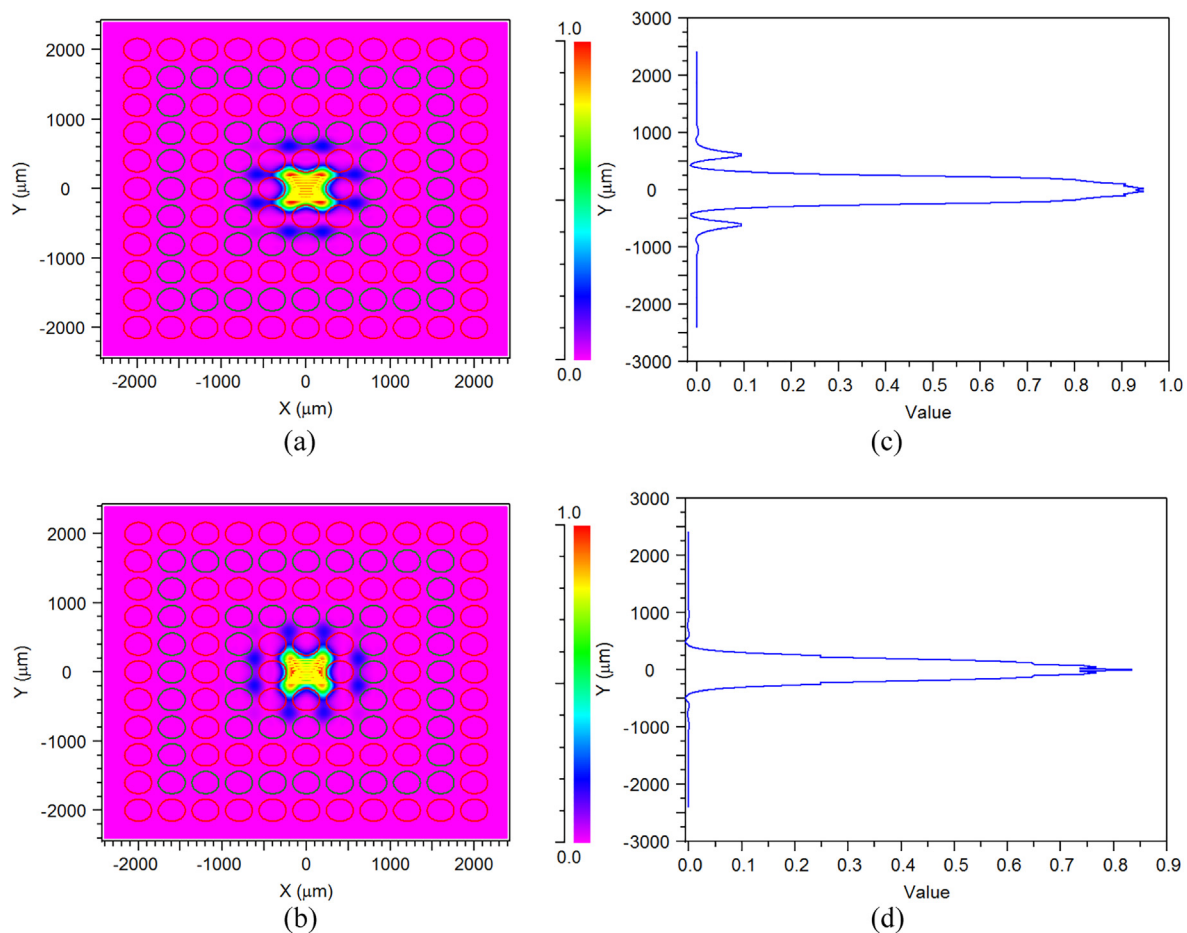


**Fig. 7** Mode fundamental field distribution of (a) x- and y-polarization (b) for the proposed PCF. Vertical cut of (c) x-mode and (d) y-mode profile at X = 0.

Fig. 7 shows the electric field distribution of x- and y- polarization of the designed PCF for optimal structure parameters. From Fig. 7(a) and 7(b), the optical field is well confined at the fiber core, meaning that the elliptical microarray-core can cause an index the difference between x- and y-polarization modes because of their asymmetrical structure. Fig. 7(c) and 7(d) show vertical cut of mode profile at X = 0.

## 4. Conclusion

The paper designs a kind of new TOPAS®-based PCF that can operate in the band of Terahertz. By making the elliptical air holes and circular air holes in the core and cladding regions, the PCF is well designed. The newly designed PCF shows significant near-zero flat dispersion property and high birefringence property. The former one has a good parameter of 0. 29 $\pm$ 0.16 ps/THz/cm, which could be well applied in multichannel communication where different optical pulses may have nearly equal pulse broadening. The latter one has a high birefringence of $1.6 \times 10^{-3}$ and ultra-low confinement loss of $3.78 \times 10^{-10}$ dB/m, which could be widely applied for polarization maintaining application, particularly for filter and sensor application. As it can be produced with the existing fiber technology, it would be put in to commercial use. Therefore, this PCF has a good prospect for next generation terahertz research.

## Declaration of Competing Interest

The authors declare that they have no known competing financial interests or personal relationships that could have appeared to influence the work reported in this paper.

## Acknowledgments

## References

[1] W. Duan, J. Gu, M. Wen, G. Zhang, Y. Ji, S. Mumtaz, Emerging Technologies for 5G-IoV Networks: Applications, Trends and Opportunities, IEEE Network 34 (5) (2020) 283–289.

[2] J. Takayanagi, H. Jinno, S. Ichino, K. Suizu, M. Yamashita, T. Ouchi, S. Kasai, H. Ohtake, H. Uchida, N. Nishizawa, K. Kawase, High-resolution time-of-flight terahertz tomography using a femtosecond fiber laser, Opt. Express 17 (9) (2009) 7533–7539.

[3] A. Arifin, N. Agustina, S. Dewang, I. Idris, D. Tahir, Polymer optical fiber-based respiratory sensors: various designs and implementations, J. Sens. vol. 2019, Article ID 6970708, 6 pages, 2019.

[4] R. Zhao, G. Lu, H. Yin, J. Liang, D. Zeng, H. Xiao, Terahertz sensor study based on spoof surface plasmon polaritons, Int. J. Antennas Propagation, vol. 2020, Article ID 2504626, 13 pages, 2020.

[5] K. Tian, J. Li, X. Yang, A novel method of micro-doppler parameter extraction for human monitoring terahertz radar network, Ad Hoc Netw. 58 (2017) 222–230.

[6] R. Islam, S. Habib, G.K.M. Hasanuzzaman, S. Rana, M.A. Sadath, C. Markos, A novel low-loss diamond-core porous fiber for polarization maintaining terahertz transmission, IEEE Photonics Technol. Lett. 28 (14) (2016) 1537–1540.

[7] N. Krumbholz, K. Gerlach, F. Rutz, Omnidirectional terahertz mirrors: A key element for future terahertz communication systems, Appl. Phys. Lett. 88 (20) (2006) 202905.

[8] C.D. Stoik, M.J. Bohn, J.L. Blackshire, Nondestructive evaluation of aircraft composites using transmissive terahertz time domain spectroscopy, vol. 16, no. 21, pp. 17039-17051, 2008.

[9] J. Bai, M. Ge, S. Wang, Y. Yang, Y. Li, S. Chang, Characteristics of a liquid-crystal-filled composite lattice terahertz bandgap fiber, Opt. Commun. 419 (2018) 8–12.

[10] B.K. Paul, K. Ahmed, Highly birefringent TOPAS based single mode photonic crystal fiber with ultra-low material loss for Terahertz applications, Opt. Fiber Technol. 53 (2019) 102031.

[11] J. Yuan, T. Ning, H. Li, L. Pei, J. Li, J. Zheng, L. Wan, Terahertz filters based on subwavelength polymer waveguide, Results Phys. 13 (2019) 102198.

[12] A. Kumar, M. V. Kartukeyan, A design of a terahertz microstrip bandstop filter with defected ground structure, Active and Passive Electronic Components, vol. 2013, Article ID 192018, 5, 2013.

[13] I.K. Yakasai, P.E. Abas, H. Suhaimi, F. Begum, Low loss and highly birefringent photonic crystal fibre for terahertz applications, Optik 206 (2020) 164321.

[14] Q. Xu, K. Li, N. Copner, S. Lin, An ultrashort wavelength multi/demultiplexer via rectangular liquid-infiltrated dual-core polymer optical fiber, Materials 12 (10) (2019) 1709, https://doi.org/10.3390/ma12101709.

[15] Y. Zhu, X. Huang, Q. Ke, G. Liu, C. Rao, D. Kong, S. Mei, Y. Liu, H. Wang, Low loss and polarization-insensitive coupling length for a terahertz fiber directional coupler with symmetric dual-suspended core structure, Opt. Commun. 480 (2021) 126497.

[16] U.F.S. Roggero, H.E. Hernández-Figueroa, Polymeric power splitters for multiplexing optical biosensors, Opt. Laser Technol. 127 (2020) 106127.

[17] B. Wang, F. Tian, G. Liu, R. Bai, L. Li, X. Yang, J. Zhang, A dual-core fiber for tunable polarization splitters in the terahertz regime, Opt. Commun. 480 (2021) 126463.

[18] J. Sultana, M.S. Islam, K. Ahmed, A. Dinovitser, B.-W.-H. Ng, D. Abbott, Terahertz detection of alcohol using a photonic crystal fiber sensor, Appl. Opt. 57 (10) (2018) 2426–2433.

[19] V.S. Chaudhary, D. Kumar, TOPAS based porous core photonic crystal fiber for terahertz chemical sensor, Optik 223 (2020) 165562.

[20] M. Abdullah-Al-Shafi, S. Sen, Design and analysis of a chemical sensing octagonal photonic crystal fiber (O-PCF) based optical sensor with high relative sensitivity for terahertz (THz) regime, Sens. Bio-Sens. Res. 29 (2020) 100372.

[21] J. Qin, B. Zhu, Y. Du, Z. Han, Terahertz detection of toxic gas using a photonic crystal fiber, Opt. Fiber Technol. 52 (2019) 101990.

[22] J. Sultana, M.S. Islam, J. Atai, M.R. Islam, D. Abbott, Near-zero dispersion flattened, low-loss porous-core waveguide design for terahertz signal transmission, Opt. Eng 56 (7) (2017) 076114, https://doi.org/10.1117/1.OE.56.7.076114.

[23] M.R. Islam, M.F. Kabir, K.M.A. Talha, M.S. Islam, A novel hollow core terahertz refractometric sensor, Sens. Bio-Sens. Res. 25 (2019) 100295.

[24] J.C. Knight, Photonic crystal fiber, Nature 424 (2003) 847–851.

[25] P. Russell, Photonic crystal fiber, Science 299 (5605) (2003) 358–362.

[26] M. Chen, R. Yu, A. Zhao, Highly birefringence rectangular lattice photonic crystal fiber, J. Opt. A: Pure Appl. Opt. 6 (10) (2004) 997–1000.

[27] S. Kim, C.-S. Kee, C.G. Lee, Modified rectangular lattice photonic crystal fibers with high birefringence and negative dispersion, Opt. Express 17 (10) (2009) 7952, https://doi.org/10.1364/OE.17.007952.

[28] S. Kim, C. Kee, J. Lee, Y. Jung, H. Choi, K. Oh, Ultrahigh birefringence of elliptic core fiber with irregular air holes, J. Appl. Phys. 101 (1) (2007) 016101.

[29] Q. Xu, R. Miao, Y. Zhang, Highly nonlinear low-dispersion photonic crystal fiber with high birefringence, Opt. Mater. 35 (2) (2012) 217–221.

[30] Q. Xu, Highly nonlinear dispersion-flattened photonic crystal fiber with high birefringence, J. Nanoelectron. Optoelectron. 8 (3) (2013) 306–310.

[31] A. Ferrando, J.J. Miret, Sing-polarization sing-mode intraband guidance in supersquare photonic crystals fibers, Appl. Phys. Lett. 78 (21) (2001) 3184–3186.

[32] A. Ferrando, E. Silvestre, J.J. Miret, P. Andrés, M.V. Andrés, Donor and acceptor guided modes in photonic crystal fibers, Opt. Lett. 25 (18) (2000) 1328, https://doi.org/10.1364/OL.25.001328.

[33] G.P. Agrawal, Nonlinear fiber optics, Academic Press, New York, 2001.

[34] M.D. Feit, J.A. Fleck, Light propagation in graded-index optical fiber, Appl. Opt. 17 (24) (1978) 3990–3998.

[35] J. Xiao, X. Sun, A Modified full-vectorial finite-difference beam propagation method based on H-fields for optical waveguides with step-index profiles, Opt. Commun. 266 (2) (2006) 505–511.

[36] K. Xie, A.D. Boardman, M. Xie, Y.J. Yang, H.M. Jiang, H.J. Yang, G.J. Wen, J. Li, K. Chen, F.S. Chen, Simulation of longitudinally magnetized three-dimensional magneto-optical devices by a full-vectorial beam propagation method, Opt. Commun. 281 (12) (2008) 3275–3285.

[37] W.P. Huang, C.L. Xu, Simulation of three-dimensional optical waveguides by a full-vector beam propagation method, IEEE J. Quantum Electron. 29 (10) (1993) 2639–2648.

[38] F. Fogli, G. Bellanca, P. Bassi, TBC and PML conditions for 2D and 3D BPM: a comparison, Opt. Quant. Electron. 30 (1998) 443–456.

[39] T.P. White, B.T. Kuhlmey, R.C. Mcphedran, D. Maystre, G. Renversez, C.M.D. Sterke, L.C. Botten, Multipole method for microstructured optical fibers. I. Formulation: errata, J. Opt. Soc. Am. B 19 (10) (2002) 2322–2330.

[40] B.T. Kuhlmey, T.P. White, G. Renversez, D. Maystre, L.C. Botten, C.M. Sterke, R.C. McPhedran, Multipole method for microstructured optical fibers. II. implementation and results, J. Opt. Soc. Am. B 19 (10) (2002) 2331–2340.

[41] T. White, R. McPhedran, L. Botten, G. Smith, C.M. de Sterke, Calculations of air-guided modes in photonic crystal fibers using the multipole method, Opt. Express 9 (13) (2001) 721, https://doi.org/10.1364/OE.9.000721.

[42] M. Koshiba, K. Saitoh, Structural dependence of effective area and mode field diameter for holey fibers, Opt. Express 11 (15) (2003) 1746–1756.

[43] M. Koshiba, K. Saitoh, Numerical verification of degeneracy in hexagonal photonic crystal fibers, IEEE Photon. Technol. Lett. 13 (12) (2001) 1313–1315.

[44] G. Su, A. Zhang, Three-dimensional finite element numerical simulation and analysis of solid-state processing of metal material, Complexity, vol. 2020, Article ID 8819745, 12 pages, 2020.

[45] V. Rastogi, K.S. Chiang, Holey optical fiber with circularly distributed holes analyzed by the radial effective-index method, Opt. Lett. 28 (24) (2003) 2449–2451.

[46] J.C. Knight, T.A. Birks, P. St, J. Russell, J.P. de Sandro, Properties of photonic crystal fiber and the effective index model, J. Opt. Soc. Am. A 15 (3) (1998) 748–752.

[47] Z. Zhu, T.G. Brown, Analysis of the space filling modes of photonic crystal fibers, Opt. Express 8 (10) (2001) 547–554.

[48] J. Arriaga, J.C. Knight, P. St, J. Russell, Modeling the propagation of light in photonic crystal fibers, Physica D 189 (1–2) (2004) 100–106.

[49] Z. Zhu, T.G. Brown, Full-vectorial finite-difference analysis of microstructured optical fibers, Opt. Express 10 (17) (2002) 853–864.

[50] M. Qiu, Analysis of guided modes in photonic crystal fibers using finite difference time domain method, Microwave Opt. Technol. Lett. 30 (5) (2001) 40–42.

[51] U. Møller, H. Merbold, J.R. Folkenberg, P.U. Jepsen, "Determination of alcohol concentration in aqueous solutions and food analysis using reflection terahertz time-domain spectroscopy, Optical Terahertz Sci. Technol. MB (2007) 18–21.

[52] W. Qian, C. Zhao, S. He, X. Dong, S. Zhang, Z. Zhang, S. Jin, J. Guo, H. Wei, High-sensitivity temperature sensor based on an alcohol-filled photonic crystal fiber loop mirror, Opt. Lett. 36 (9) (2011) 1548–1550.

[53] D. Wang, G. Chen, L. Wang, Thermal tunability of photonic bandgaps in liquid crystal filled polymer photonic crystal fiber, Opt. Fiber Technol. 29 (2016) 95–99.

[54] A. Argyros, Microstructured polymer optical fibers, J. Lightwave Technol. 27 (11) (2009) 1571–1579.

[55] G. Khanarian, Optical properties of cyclic olefin copolymers, Opt. Eng. 40 (6) (2001) 1024–1029.

[56] M.R. Hasan, M.A. Islam, M.S. Anower, S.M.A. Razzak, low-loss and bend-insensitivity terahertz fiber using a rhombic-shape core, Appl. Opt. 55 (30) (2016) 8441–8447.

[57] S. Asaduzzaman, K. Ahmed, T. Bhuiyan, T. Farah, Hybrid photonic crystal fiber in chemical sensing, SpringerPlus 5 (1) (2016), https://doi.org/10.1186/s40064-016-2415-y.

[58] S. Asaduzzaman, K. Ahemd, Microarray-core based circular photonic crystal fiber for high chemical sensing capacity with low confinement loss, Optica Applicata vol. XLVII, no. 1, pp. 41-49, 2017.

[59] S. Asaduzzaman, K. Ahmed, Proposal of a gas sensor with high sensitivity, birefringence and nonlinearity for air pollution monitoring, Sens. Bio-Sens. Res. 10 (2016) 20–26.

[60] M.A. Habib, M.S. Anower, Low loss highly birefringent porous core fiber for single mode terahertz wave guidance, Curr. Opt. Photon. 2 (3) (2018) 215–220.

[61] M.F.H. Arif, K. Ahemd, S. Asaduzzaman, M.A.K. Azad, Design and Optimization of photonic crystal fiber for liquid sensing application, Photonic Sens. 6 (2016) 279–288.

[62] S. Rana, N. Kandadai, H. Subbaraman, A highly sensitive, polarization maintaining photonic crystal fiber sensor operating in the THz regime, Photonic 5 (2018) 41–49.

[63] S. Goudarzi, N. Kama, M.H. Anisi, S. Zeadally, S. Mumtaz, Data collection using unmanned aerial vehicles for Internet of Things platforms, Comput. Electr. Eng. 75 (2019) 1–15.

[64] J. Li, Z. Zhou, J. Wu, J. Li, S. Mumtaz, X.i. Lin, H. Gacanin, S. Alotaibi, Decentralized On-Demand Energy Supply for Blockchain in Internet of Things: A Microgrids Approach, IEEE Trans. Comput. Social Syst. 6 (6) (2019) 1395–1406.